Delgado-Muñoz, D.; Fernández-Arroyo, A.; Domine, ME.; García-González, E.; López Nieto, JM. (2019). W-Nb-O oxides with tunable acid properties as efficient catalysts for the transformation of biomass-derived oxygenates in aqueous systems. Catalysis Science & Technology. 9(12):3126-3136. https://doi.org/10.1039/c9cy00367c

# W-Nb-O oxides with tunable acid properties as efficient catalysts for the transformation of biomass-derived oxygenates in aqueous systems

Daniel Delgado,[a] Alberto Fernández-Arroyo,[a] Marcelo E. Domine,[a,*] Ester García-González,[b] and José M. López Nieto[a,*]

[a)] Instituto de Tecnología Química, Universitat Politècnica de València-Consejo Superior de Investigaciones Científicas, Avenida de los Naranjos s/n, 46022 Valencia (Spain). E-mail: jmlopez@itq.upv.es, mdomine@itq.upv.es

[b)] Departamento de Química Inorgánica, Facultad de Ciencias Químicas, Universidad Complutense, 28040 Madrid, Spain.

**Abstract**

W-Nb-O oxide bronzes, prepared hydrothermally, have been characterized and studied as catalysts for both the gas phase dehydration of glycerol and the liquid phase selective condensation of light oxygenates derived from primary treatments of biomass (a mixture containing acetic acid, ethanol, propanal, hydroxyacetone and water). By controlling the nominal composition of the catalysts it is possible to tune up their textural and acid properties (concentration and nature of acid sites) to selectively produce acrolein from glycerol or $C_5$-$C_{10}$ hydrocarbons (with low O contents) and in high yields) from light oxygenates. Interestingly, these catalysts are stable when working in gas phase reaction and they are re-usable, with high resistance to leaching, when working in aqueous media.

## INTRODUCTION

Second generation biomass feedstocks constitute one of the main sustainable and renewable alternatives to fossil sources for the production of commodity chemicals and fuels.[1-5] Regarding the new bio-economy concept, the valorization of some types of waste streams is a key point in the development of bio-refineries. This is the case of glycerol (formed during the biodiesel production)[6-9] or the aqueous fraction containing low-value short-chain oxygenates (residues generated from lignocellulosic biomass fast pyrolysis)[10-14]. For some specific reactions, solid acids seem to be the most interesting catalysts for the selective transformation of both residues.

Glycerol can be selectively transformed into acrolein, an important intermediate in the chemical industry.[6-9] This reaction can be carried out over solid acid catalysts by a dehydration mechanism,[6-9,15-20] in which Brønsted acid sites seem to be more active and selective than Lewis acid sites.[17-20] Several types of materials have been proposed as catalysts for this reaction in the last decade,[4-7] including W-containing materials (both bulk and supported ones).[17-20] In this sense, tungsten-based metal oxide bronzes, especially the hexagonal tungsten bronze (*h*-$WO_3$), show interesting catalytic performance for this reaction; although the addition of promoters can modify the reaction products obtained: i) pure *h*-$WO_3$ and Nb-modified *h*-$WO_3$ to selectively form acrolein;[7,21-24] and ii) vanadium and/or molybdenum modified *h*-$WO_3$ to form acrylic acid in one-pot.[7,25-28] Moreover, and although dehydration can be carried out in inert atmosphere, it has been reported that, in many cases, the presence of oxygen in the feed has a beneficial effect to avoid catalyst decay.[18,19]

On the other hand, aqueous fraction containing low-value short-chain oxygenates (aldehydes, ketones, alcohols, among others), derived from the fast pyrolysis of lignocellulosic biomass, could be upgraded by C-C bond formation reactions like

ketonization or aldol condensation, increasing their carbon chain length and reducing oxygen content.[29-31] In this way, catalysts based on CeZrO oxide have been widely studied for the ketonization of small aldehydes in the presence of water or acetic acid,[32] whereas $ZrO_2$ or $TiO_2$ have been considered for the aldol condensation using acetic acid or propanal as probe molecules.[33] Interestingly, both acids and bases are able to catalyze C-C bond formation reactions, leading to similar product distributions through different reaction mechanisms. In all these cases, the catalytic performance is explained in terms of structural features and specific acid-base properties of the materials. Recently, it has been proposed that niobium oxide based catalysts show interesting catalytic performance in C-C bond formation reactions.[34, 35]

Bronze-type materials include a vast group of closely related structural phases with the ability of accommodating wide variation range of chemical composition.[22-26,36-42] These facts open up the possibility to modulate their specific functionalities. In addition, alternative synthetic routes for obtaining these phases, (like hydrothermal, reflux or evaporation methods) have been proposed, what has made it possible to produce materials with surface areas suitable for catalytic applications. [22-24, 36-44]

Herein we report the synthesis of a series of W-Nb mixed oxides obtained by the hydrothermal method, which present bronze-type structures and tailored acid and textural properties. Materials have been tested as catalysts in both the gas phase aerobic transformation of glycerol to acrolein and in the transformation of light oxygenated compounds present in an aqueous model mixture, resembling that of a waste effluent at a bio-refinery. The effect of Nb-content in both their physicochemical properties and catalytic performance is discussed in detail, especially in terms of its effect on the crystal structure, textural and acid properties, and on the catalytic behavior.

## EXPERIMENTAL

### Synthesis of materials

W-Nb-O mixed oxides were synthesized from acidified aqueous solutions containing stoichiometric amounts ($H_2O$/(W+Nb) molar ratio: 53/1) of the corresponding metal salts: ammonium metatungstate hydrate (≥85 wt% $WO_3$ basis, Sigma–Aldrich) and niobium oxalate monooxalate adduct (ABCR). These solutions were introduced into Teflon-lined stainless steel autoclaves, purged with $N_2$ and finally treated at 175 ºC during 48 h. Resulting solids were filtered off, washed with distilled water and dried at 100 ºC for 16 h. Finally, they were heat-treated at 550 ºC under $N_2$ flow (15 ml $g_{cat}^{-1}$) during 2 h. The catalysts are named as WNb-x, being x the corresponding Nb/(W+Nb) atomic ratio in solids (measured by XEDS). Table 1 shows the main physico-chemical characteristics of catalysts.

**Table 1**

Undoped tungsten oxide sample (named as WNb-0) was just heat-treated at 450ºC to avoid the transformation into *m*-$WO_3$ (see below).[28] Pure niobium oxide was synthesized from an aqueous solution ($H_2O$/Nb molar ratio: 53/1) following the process described above (final heat-treatment temperature of 550 ºC).[34]

### Catalyst Characterization

Powder X-Ray diffraction (XRD) patterns were obtained in a PANalytical X´Pert PRO diffractometer using CuKα radiation and an X´Celerator detector in a Bragg-Brentano geometry.

Raman spectra were recorded at ambient temperature in an inVia Renishaw spectrometer equipped with an Olympus microscope, a CCD detector and a Renishaw HPNIR laser.

An exciting wavelength of 514 nm was used, with an approximated power of 15 mW on the samples.

In order to obtain the bulk composition of the catalysts energy-dispersive X-ray spectroscopy (XEDS) was performed in a JEOL 6300 scanning electron microscope, with an Oxford LINK ISIS detector connected. Counting time used for each spectrum was 100 s.

Samples for transmission electron microscopy (TEM) were ultrasonically dispersed in *n*-butanol and transferred to carbon coated copper grids. Selected area electron diffraction (SAED) and high resolution transmission electron microscopy (HRTEM) were performed on a JEOL JEM300F electron microscope working at 300 kV (point resolution of 0.17 nm). XEDS crystal-by-crystal chemical microanalysis was performed in the same microscope equipped with an ISIS 300 X-ray microanalysis system (Oxford Instruments) with a detector model LINK "Pentafet" (resolution 135 eV).

$N_2$ adsorption isotherms were collected in a Micromeritics ASAP 2000. Samples were degassed in vacuum at 300 ºC. Surface areas were calculated by Brunauer-Emmett-Teller (BET) method. Pore size distributions and pore volumes were obtained by Barrett-Joyner-Halenda (BJH) method.

Infrared spectra of adsorbed pyridine were recorded in a Nicolet 710 spectrometer, where self-supported wafers of 10 mg $cm^{-2}$ were degassed in vacuum ($10^{-2}$ Pa) at 200 ºC during 12 h. Afterwards, pyridine was admitted ($6.5x10^2$ Pa) and, after achieving equilibrium, samples were outgassed at 150 ºC and cooled down to room temperature. IR spectra were then acquired. The IR spectra recorded before pyridine adsorption were used as a background for pyridine-adsorbed spectra. This background was subtracted from each spectrum by difference, and the absorbance was normalized to weight before

calculations. Concentration of acid sites was calculated from band intensities (signals at ca. 1545 and 1450 $cm^{-1}$ for Brönsted and Lewis sites, respectively) and extinction coefficients, applying a method previously proposed.[45]

Temperature-programmed desorption of ammonia (TPD-$NH_3$) was carried out in a Micromeritics TPD/2900 device. Samples were pre-treated at 350 ºC under He flow during 1h. Then, chemisorption of $NH_3$ was performed by pulses at 100 ºC. After treating the samples with He stream during 15 min (to eliminate physisorbed ammonia), temperature was increased gradually (10 ºC $min^{-1}$) up to 500 ºC. Desorbed ammonia was monitored by following $NH_3$ characteristic mass of 15 a.m.u. (atomic mass unit) by mass spectrometry.

**Catalytic tests for glycerol dehydration**

The gas phase transformation of glycerol was carried out at atmospheric pressure in a fixed-bed reactor at 295 °C. The feed consisted of a mixture glycerol-water-oxygen-helium with a molar ratio of 2/40/4/54 using a contact time, W/F, of 81 $g_{cat}$ h $(mol_{GLY})^{-1}$. The effluent stream was bubbled through a condenser device at 0 – 3 °C, while the remaining gaseous products were analyzed by online gas chromatography (HP 6890) equipped with two chromatographic columns: [45] i) a molecular sieve 5Å (3.0 m length); and ii) a Porapak Q (3.0 m length) column. The condensed liquids were analyzed by gas chromatography in a Varian 3900 chromatograph equipped with a 100% dimethylpolysiloxane capillary column (100 m× 0.25 mm× 0.5).

**Catalytic tests for condensation reaction**

Catalytic experiments were performed in a 12 ml autoclave-type reactor with PEEK (polyether-ethyl-ketone) interior, equipped with a magnetic bar, pressure control and a

valve for either liquid or gas sample extraction. Reactors were placed over a steel jacket individual support equipped with a temperature close loop control system.

The initial feed consisted of an aqueous model mixture containing short-chain oxygenated compounds. In all the cases the following composition has been used: water (30 wt%), acetic acid (30 wt%), propanal (25 wt%), acetol (5 wt%) and ethanol (10 wt%). The composition simulates that of a waste stream derived from the aqueous phase separation of a pyrolytic bio-oil. Typically, 3.0 g of aqueous model mixture and 0.15 g of catalyst were introduced in the autoclave-type reactor. The reactor was sealed, pressurized at 13 bar of $N_2$ and heated at 180-200 ºC under continuous stirring.

Small liquid aliquots (50-100 µl) were taken at different time intervals, filtered off and diluted in 0.5 g of methanol containing 2 wt% chlorobenzene as standard. The liquid samples were analyzed by a Bruker 430 GC equipped with a FID detector and a capillary column (TRB-624, 60m length).

Reactants and intermediate products were quantified from GC-FID. Product identification was done by GC-MS (Agilent 6890 N GC System coupled with an Agilent 5973 N mass detector and equipped with a HP-5 MS, 30 m length capillary column) (Figure S1). A further explanation of the experimental part and calculations is shown in the Supporting Information.

## RESULTS AND DISCUSSION

### Catalyst Characterization

Powder-XRD patterns of hydrothermal W-Nb-O mixed oxides are depicted in Figure 1A. Pattern *a*, corresponding to WNb-0 catalyst, can be assigned to the hexagonal

tungsten bronze-type structure *h*-$WO_3$ (HTB, ICDD: 00-33-1387), in which $WO_6$ octahedra share their vertices along the three crystallographic directions, displaying trigonal and hexagonal channels along c-axis (Figure 1B).[21] Isomorphic substitution of W by Nb causes the progressive loss of crystallinity and important changes in the corresponding diffraction patterns occur for these materials (Figure 1A, patterns *b*-*h*). For Nb/(W+Nb) ratios lower than 0.5, catalysts preserve the HTB crystal structure, although the intensity of diffraction maxima becomes notably lower (Figure 1A, patterns *b* and *c*). The crystallinity loss results in a rapid decrease in the intensity of the diffraction maxima. For Nb/(W+Nb) ratios higher than 0.5, broad and ill-defined diffraction maxima at 2θ values of ca. 27˚, 35˚, 50˚ and 55˚ are present but, the XRD patterns are dominated by two diffraction maxima at 2Θ ~ 22 and 46° (Figure 1A, *d*-*h*). These two diffraction maxima are assigned to the (001) and (002) reflections of the HTB structure and the observed transformation can be explained from the progressive loss of the long range order in the *ab* plane of the structure, that gives rise to the formation of the hexagonal and trigonal tunnels, while keeping inter-octahedral connectivity. In fact, they can correspond to the (001) and (002) *d* spacing of any structure derived from a corner sharing octahedral framework with a basic unit cell parameter of about 3.8Å and thus, accounting for the octahedral interconnectivity. The tungsten/niobium ratio plays a crucial role in the stabilization of *h*-$WO_3$ and the introduction of Nb finally gives rise to a pseudo-crystalline mixed oxide phase already observed in other Mo, Nb and W-based mixed oxides.[25, 46, 47] The magnitude of the *c*-axis, considered as the sharing corner-connection between octahedra was calculated from the (001) diffraction maximum (Figures 1B and 1C). It can be noticed that *c* parameter increases linearly with Nb content up to Nb/(W+Nb) ratio of 0.53, which is consistent with the relative ionic size of both elements ($r^{VI}Nb^{5+}$= 0.64 Å, $r^{VI}W^{6+}$ = 0.60

Å).[48] For higher Nb-content, *c*-axis remains almost constant and it is important to mention that the interval of composition for which no variation of *c* is observed, corresponds to catalysts that are pseudo-crystalline.

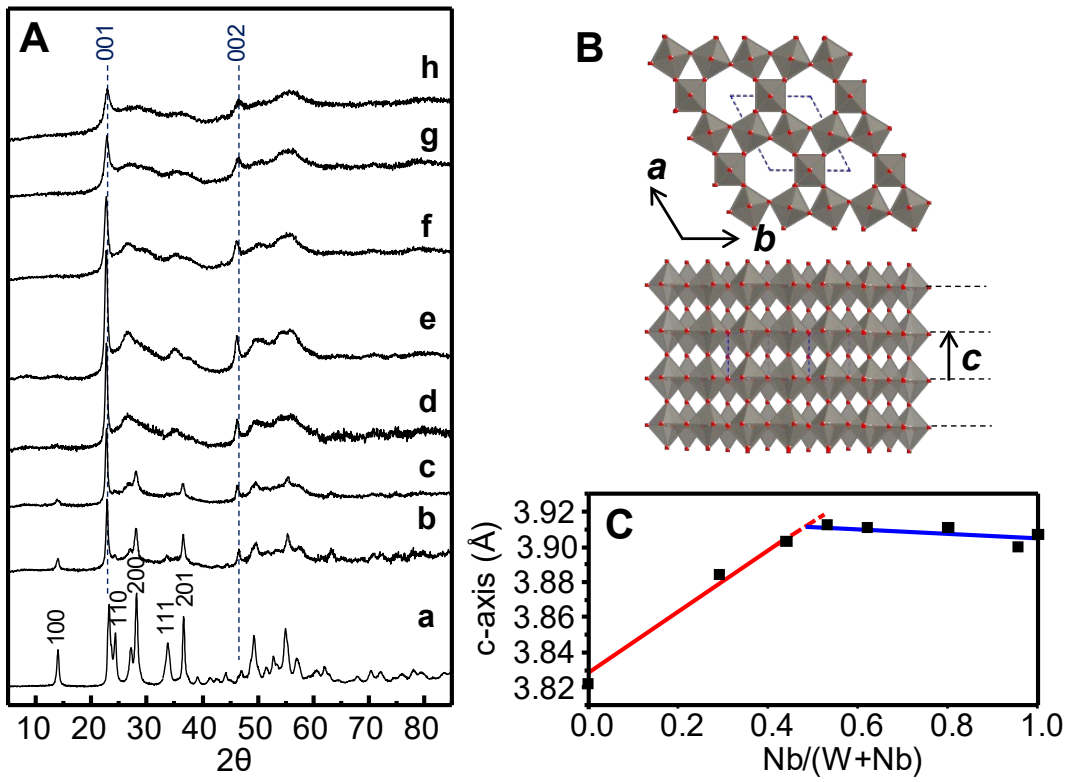


**Figure 1.** A) XRD patterns of W-Nb-O catalysts: a) WNb-0; b) WNb-0.29; c) WNb-0.40; d) WNb-0.53; e) WNb-0.62; f) WNb-0.80; g) WNb-0.95; h) WNb-1. Miller indices have been assigned according to the hexagonal $WO_3$ phase (*h*-$WO_3$, ICDD: 00-33-1387). B) Projected structural model of the *h*-$WO_3$ structure along the [001] and [210] directions. C) Variation of c-axis as a function of Nb content.

Figure 2 shows the Raman spectra of W-Nb-O catalysts. Pure tungsten oxide bronze (sample WNb-0) presents the characteristic bands of *h*-$WO_3$: those centered at 780, 691 and 648 $cm^{-1}$, being assigned to O-W-O stretching vibration; and bands at 331, 291 and 261 $cm^{-1}$, attributed to O-W-O deformation mode (Figure 2 *a*).[41,49]

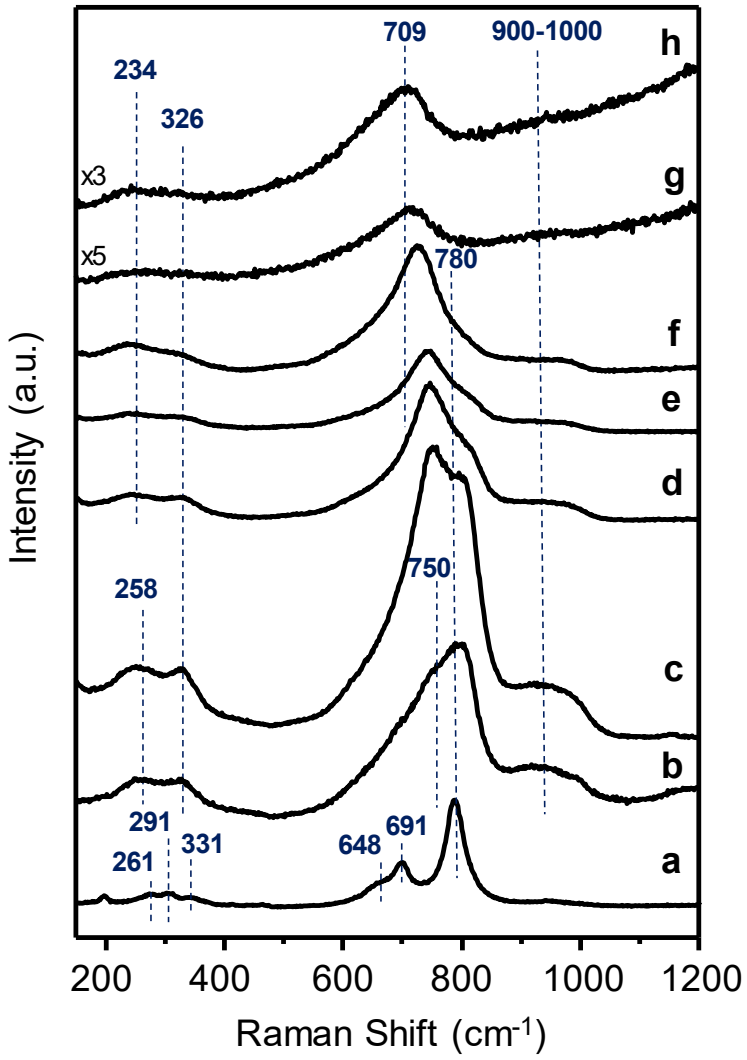


**Figure 2.** Raman spectra of W-Nb-O catalysts: a) WNb-0; b) WNb-0.29; c) WNb-0.40; d) WNb-0.53; e) WNb-0.62; f) WNb-0.80; g) WNb-0.95; h) WNb-1.

The partial substitution of Nb for W gives rise to a new broad signal at 900-1000 $cm^{-1}$, which is related to M=O type stretching vibrations (M = W, Nb) (Figure 2, *b*-*h*),[50-51] whereas the intensity of the band at 780 $cm^{-1}$ progressively decreases. Likewise, a new band at 750 $cm^{-1}$ is observed (Figure 2 *b*), which progressively shifts to 709 $cm^{-1}$ as Nb content in the catalyst increases (Figure 2, *b*-*h*). The band at 709 $cm^{-1}$ has been ascribed to symmetric stretching mode of slightly distorted $NbO_6$ octahedra in bulk niobium

oxides and its shift is consistent with the progressive Nb-enrichment along the composition range studied.[52] Additionally, bands at lower frequencies (below 400 $cm^{-1}$), related to deformation vibrational modes in the oxide, become broader, probably due to the increasing disorder in the connectivity of polyhedra. Moreover, the signal at 258 $cm^{-1}$ also shifts to 234 $cm^{-1}$ as Nb content increases, which can be attributed to Nb-O-Nb deformation modes.[53]

Due to the unclear identity of the crystal phases present, samples were further investigated by electron diffraction and high-resolution electron microscopy. For the lowest Nb content (WNb-0.29), sample is constituted by crystals of the HTB type phase (average size about 50 nm), as shown by the electron diffraction ring pattern in Figure 3a.

The corresponding high-resolution micrograph on Figure 3b shows a group of crystals representative of this sample, where characteristic *d*-spacing distances corresponding to the HTB type phase can be measured. From the crystal by crystal XEDS microanalysis performed, the atomic composition varies in the range $W_{0.82}Nb_{0.18}O_{3-x}$ – $W_{0.70}Nb_{0.30}O_{3-x}$ for the crystals of this catalyst (bulk composition $W_{0.71}Nb_{0.29}O_{3-x}$, see Table 1). Further increasing the Nb content implies a progressive loss of the order degree in the *ab* plane of the HTB structure, as well as a reduction of the average crystal size. Figure 3c shows the electron diffraction ring pattern of the WNb-0.53 sample, where the disappearance of the (100) reflection is observed. The average crystallite size is ≈10 nm and chemical heterogeneity is detected, the atomic composition varying in the range $W_{0.65}Nb_{0.35}O_{3-x}$ – $W_{0.50}Nb_{0.50}O_{3-x}$ from crystal to crystal.

Figure 3d corresponds to the high-resolution electron micrograph of a group of crystals of the same sample where *d*-spacing of about 4 Å are measured. There exists a certain

amount of bigger crystals (size >50 nm) which present low niobium content (<15%), high crystallinity and their periodicities can be assigned to the HTB type phase. At this point, it is important to mention that in WNb-0.53 and WNb-0.62 samples small crystallites (≈5 nm) are frequently observed in which fragments of the $Cs_{0.5}Nb_{2.5}W_{2.5}O_{14}$ type phase can be clearly recognized (Figures 3e and 3f). This crystal phase is isostructural with the well-known M1-phase, widely studied for the ethane ODH[40] and the partial oxidation of propane.[54]

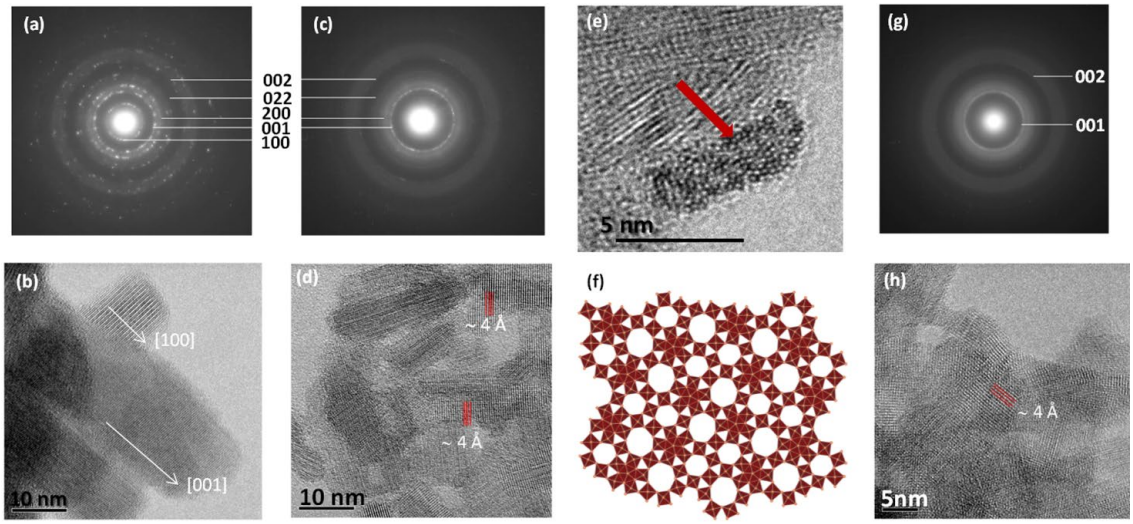


**Figure 3.** (a) Electron diffraction ring pattern for the WNb-0.29 sample; (b) High resolution image showing a group of representative crystals of WNb-0.29; (c) Electron diffraction ring pattern for the WNb-0.53 sample; (d) High resolution micrograph showing several crystallites of this catalyst; (e) High resolution image showing one crystallite (pointed by the red arrow) in which fragments of the $Cs_{0.5}Nb_{2.5}W_{2.5}O_{14}$ type phase can be recognized; (f) Projected structure model of $Cs_{0.5}Nb_{2.5}W_{2.5}O_{14}$ type phase along the [001] direction; (g) Electron diffraction ring pattern corresponding to the WNb-0.80 sample; (h) High resolution image showing several crystallites of WNb-0.80. Miller index in all diffraction patterns have been assigned on the basis of the HTB-type phase (ICDD: 00-33-1387).

The Nb:W ratio close to 1 seems to favor the formation of the structural framework of the mentioned crystal phase in these catalysts. The coexistence of all these different crystal phases is compatible with the X-ray diffraction patterns of the corresponding samples, and the presence of $Cs_{0.5}Nb_{2.5}W_{2.5}O_{14}$ type phase can be inferred from the faint and broad diffraction maxima at 2θ values of ca. 8˚ (see Figure 1A, patterns *d* and *e*). In samples with high Nb-contents, i.e. from WNb-0.80 to WNb-1, the formation of the $Cs_{0.5}Nb_{2.5}W_{2.5}O_{14}$ type phase is not observed. Figure 3g shows the electron diffraction ring pattern of the sample WNb-0.80 where only rings corresponding to (001) and (002) reflections are visible, other maxima being in the form of diffuse halos. Figure 3h corresponds to the high-resolution electron micrograph of a group of crystals of this catalyst and the average crystal size is slightly smaller (5-10 nm). Samples from WNb-0.62 to WNb-1 are chemically homogeneous from crystal to crystal with compositions close to the nominal one, as revealed by crystal by crystal XEDS microanalysis. In this interval, samples also present uniform crystal size and crystallites appear constituting nanocrystalline agglomerates.

Textural properties of W-Nb-O mixed oxides were studied by means of $N_2$ adsorption. $N_2$-adsorption isotherms show a transition from type II (for samples with Nb/(Nb+W) lower than 0.50) to type IV (for samples with high Nb contents), which are typical of mesoporous materials (Figure S2). Indeed, these changes are accompanied by a concomitant variation in average pore sizes, pore size distributions and pore volumes (Table 1). In this sense, materials with Nb/(Nb+W) lower than 0.50 present a broad size distribution whereas for higher Nb concentrations narrower distributions are observed, with pore sizes in the range 5.3-3.5 nm (Figure S3). Likewise, average pore size of the catalysts decreases from 17.2 nm for sample WNb-0 to 3.5 nm for sample WNb-1, when increasing the Nb content (Table 1). Interestingly, a drastic drop in the average

pore size (from 14.6 to 5.9 nm) is observed when Nb content exceeds ca. 50% as further introduction of niobium also gives rise to a strong increase in the percentage of mesopores (Table 1). There is a connection between this fact and the microstructural modifications observed in this composition range, the mesoporous structure (i.e. the narrow mesopore size distributions) being related to the packed agglomeration of uniform nanoparticles.

Acid properties of the catalysts were elucidated by means of FTIR of adsorbed pyridine and temperature-programmed desorption of ammonia (TPD-$NH_3$) (Table 1) (Figures 4 and 5, and Figure S4). It is noteworthy that both techniques lead to the same trends with regard to the variation of the amount of acid sites per gram of catalyst and per catalyst surface area, at increasing Nb contents (Figure 4 and Figure S4). However, absolute values of adsorbed pyridine were much lower than the amount of adsorbed $NH_3$, likely due to steric hindrance caused by the bigger size of pyridine molecule (Figure 4 and Figure S4). Considering the concentration of acid sites in terms of the total number of acid sites per gram of catalyst, the acidity of W-Nb-O oxides increases with Nb content, reaching a maximum for Nb/(W+Nb) atomic ratios of ca. 0.8 (Figure 4a). On the contrary, the surface density of acid sites (i.e. the number of acid sites per surface area) decreases when increasing Nb content, due to the higher surface areas observed (Figure 4b). Additionally, the Brönsted/Lewis acid sites ratio (BAS/LAS) decreases when increasing the Nb-content (Figure 4c). We must inform that the lower BAS/LAS ratio observed for undoped tungsten oxide (i.e. WNb-0 sample) can be ascribed to the presence of ammonium ions in the hexagonal channels of the crystal structure, due to the lower heat-treatment temperature used for this material. The elimination of $NH_4^+$ cations after calcination has been reported to be the cause of the generation of Brönsted type acidity in bronze-type catalysts.[55]

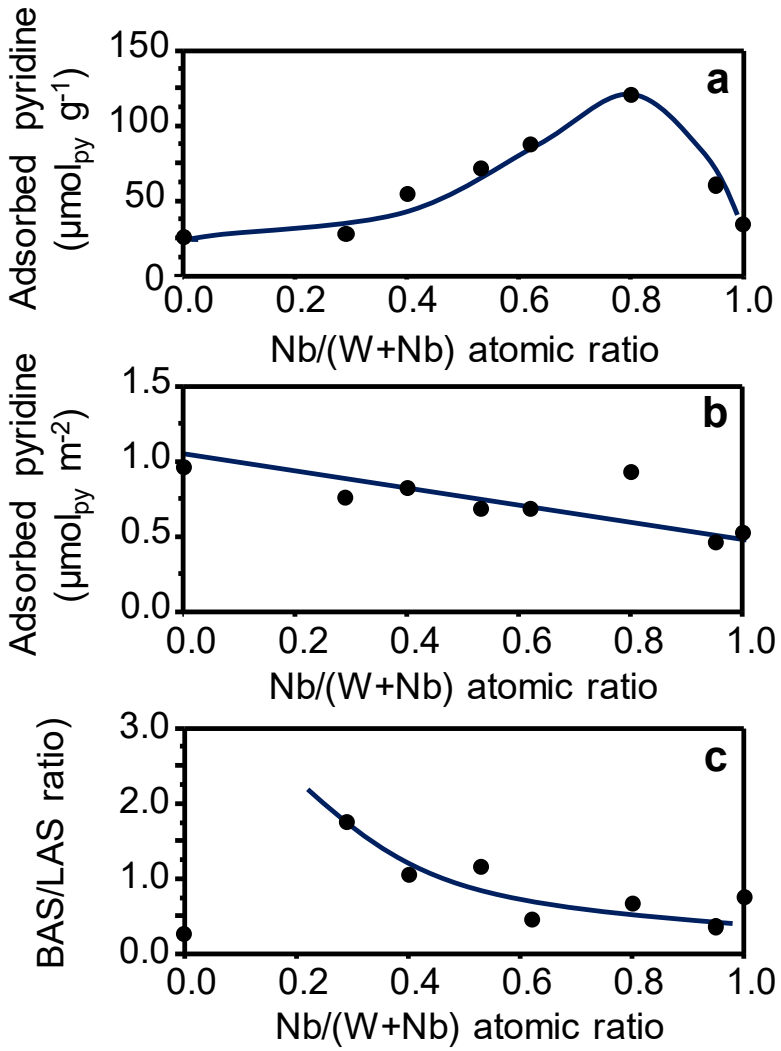


**Figure 4.** Acid features of W-Nb-O mixed oxides catalysts obtained by FTIR of adsorbed pyridine: a) Concentration of acid sites sites (in $\mu mol_{py}\ g^{-1}$); b) Surface density of acid sites (in $\mu mol_{py}\ m^{-2}$); and c) BAS/LAS ratio (BAS: Brönsted Acid Sites; LAS: Lewis Acid Sites).

Figure 5 displays TPD-$NH_3$ profiles of synthesized catalysts. All the catalysts show two main contributions to the desorption profile, at ca. 200 and 300 ºC, which can be attributed to desorption of ammonia from acid sites with low and medium-high acid strength, respectively (Figure 5). The incorporation of $Nb^{5+}$ atoms within the bronze framework leads to an increase of the relative intensity of the signal appearing at low

temperature (ca. 200 ºC), i.e. favoring an increase in proportion of low strength surface acid sites.

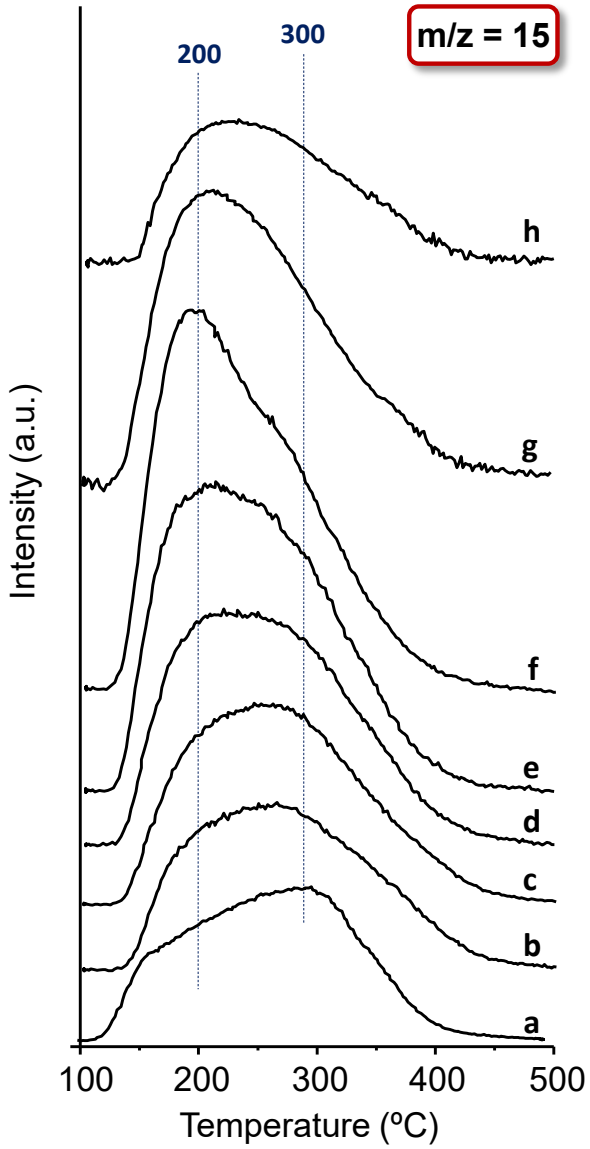


**Figure 5.** TPD-$NH_3$ profiles of W-Nb-O catalysts: a) WNb-0; b) WNb-0.29; c) WNb-0.40; d) WNb-0.53; e) WNb-0.62; f) WNb-0.80; g) WNb-0.95; h) WNb-1.

**Catalytic tests for aerobic glycerol dehydration**

W-Nb-O mixed metal oxides have been tested in the aerobic transformation of glycerol. The catalytic results are comparatively shown in Figure 6 and Table S1. Total

conversion of glycerol is observed all along the series, regardless the Nb-content. In all the cases, the main reaction product was acrolein, which is obtained via a double dehydration mechanism:[6-9] i) the removal of the internal $OH^-$ group, and ii) tautomerization-dehydration of the terminal $OH^-$ group of glycerol. Although acrolein is observed in all the cases, the selectivity to the different products is highly dependent on the Nb-content in the materials.

In addition to acrolein, heavy compounds (products that are not eluted into the gas chromatograph due to their high molecular weight) and carbon oxides, together with small amounts of acetaldehyde, acetic acid and acrylic acid (grouped as "others" in Table S1) are obtained. Thus, the selectivity to acrolein decreases when the Nb-content in the catalysts increases (Figure 6). In a parallel way, a concomitant increase in the yield to carbon oxides and heavy by-products is observed (Figure 6).

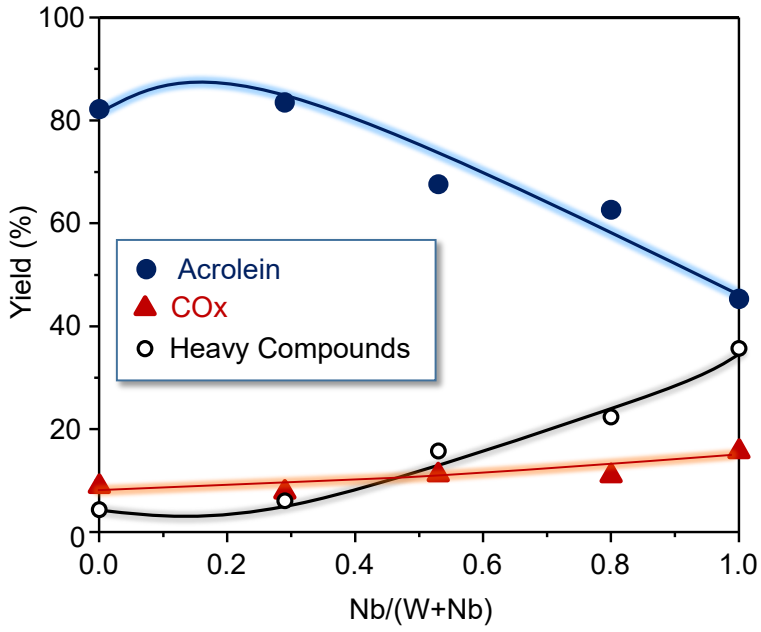


**Figure 6.** Variation of the yield to the main reaction products, acrolein, $CO_X$ and heavy-compounds, as a function of Nb content in catalyst. Reaction conditions: glycerol/$H_2O$/$O_2$/He molar ratio of 2/40/4/54, T = 295 ºC, Contact time, W/F, of 81 $g_{cat}$ h $(mol_{gly})^{-1}$.

In this sense, acid characteristics seem to control the selectivity profiles in the aerobic transformation of glycerol, being the increase in the yield to heavy compounds and carbon oxides related with the increment in the Lewis acid nature of the surface. Although both the decrease of acid strength and surface density of acid sites with Nb-content should favor the acrolein desorption, it seems that the higher concentration of Lewis sites (Figure 5) has a drastic effect in the selectivity profiles. In particular, Lewis sites (mainly $Nb^{5+}$ species) can coordinate acrolein,[16] hindering its desorption, and promoting the formation of heavy compounds and carbon oxides. Therefore, the most selective catalysts in this case are those with low Nb/(W+Nb) ratios, presenting a high proportion of Brönsted acid sites. In this way, it has been proposed that the presence of Brönsted acid sites favors de dehydration of secondary alcohol group from glycerol forming 1,3-propanediol, which after tautomerization forms 3-hydroxypropionaldehyde and finally gives acrolein.[16] However, the presence of Lewis acid sites, favors the dehydration of a primary alcohol group to form hydroxyacetone.[16]

**Catalytic activity for condensation reactions**

As shown in the previous sections, the control of Nb-content in W-Nb-O oxides allows us to obtain catalysts presenting well-defined textural properties, nature, concentration and density of acid sites. In this sense, tuning Nb content gives rise to materials with tailored physicochemical properties for a specific application. In the case of light oxygenated compounds valorization, it has been reported that Lewis acid/base pairs can assist the formation of the intermediates in ketonization and aldol condensation reactions. Meanwhile, Brönsted acid/base sites are necessary in the case of esterification

reactions.[56,57] Thus, catalysts were tested in the transformation of short-chain oxygenates present in an aqueous model mixture, which resembles that of a waste effluent at bio-refineries. The tests were performed in Teflon-lined stainless steel autoclaves under moderate temperature (180 and 200 ºC) and pressure ($P_{N2}$ = 13 bar). Results have been discussed in terms of conversion of the different oxygenated compounds and selectivity to the main condensation and/or ketonization products (i.e. 2-methyl-2-pentenal, $C_5$-$C_8$ and $C_9$-$C_{10}$ fractions) and to ethyl acetate as the main by-product (Figure S5).

$C_5$-$C_{10}$ molecules mainly come from condensation reactions among the different organic compounds present in the model aqueous mixture. In this sense, most of these compounds are derived from consecutive self-condensation reactions of propanal, as it is one of the compounds with a higher concentration in the aqueous mixture (30 wt%). Additionally, cross-condensation reactions also occur among propanal and acetol leading to a different $C_6$ compound (2,3-hexanedione) compared to the main intermediate compound (2-methyl-2-propanal) derived from propanal self-condensation. Small amounts of acetone (derived from acetic acid ketonization) are also observed, which can also react via aldol condensation with propanal and acetol. These compounds can continue reacting via condensation reactions to produce different $C_9$ compounds. Due to the complexity of this system, other reactions including cyclation, and decarbonylation, among others can also take place leading to different $C_5$-$C_{10}$ molecules. The main reaction products can be observed in Figure S5.

Figure 7a shows the variation of the conversion of each reactant in the aqueous model mixture as a function of Nb/(Nb+W) atomic ratio in catalysts, achieved at 180 ºC and a time on stream of 7h (Table 2). Conversion of acetol (100%), ethanol (37-47%) and acetic acid (13-19%) remain nearly constant regardless Nb content in the catalyst.

However, propanal conversion increases with Nb content, reaching the highest value for Nb/(W+Nb) around 0.53 (84-90%), pure tungsten oxide (WNb-0 sample) displaying the lowest conversion (61.2%) (Figure 7a, Table 2). In this way, a concomitant increment in the selectivity to 2-methyl-2-pentenal (2M2P, via self-aldol condensation of propanal, Figure S5) can be observed when increasing Nb content in the catalysts (Figure 7b). Selectivity to $C_9$-$C_{10}$ products shows the same trend, since they are mainly formed via aldol condensation of $C_5$-$C_8$ fractions with smaller molecules (Figure S5).

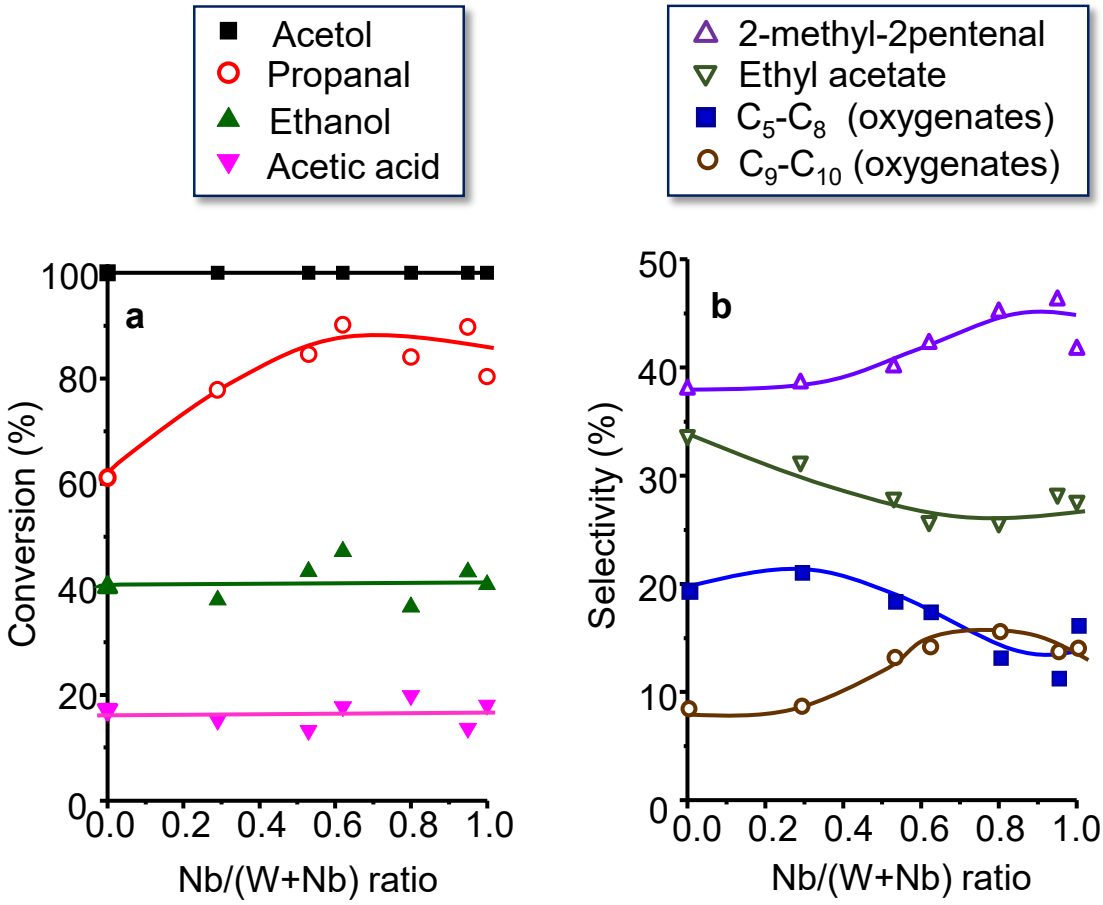


**Figure 7.** Variation of the conversion of each reactant in the aqueous model mixture (i.e. acetol, propanal, ethanol and acetic acid) (a) and variation of selectivity to the main products (i.e. 2-methyl-2-pentenal, ethyl acetate, and $C_5$-$C_8$ and $C_9$-$C_{10}$ compounds) (b) as a function of Nb content in catalyst. Reaction conditions: Aqueous model mixture (3.0 g) and catalyst (0.15 g) in autoclave-type reactor, at 13 bar $N_2$ and 180˚C under continuous stirring; time on stream of 7 h.

Consequently, the selectivity to $C_5$-$C_8$ compounds decreases when increasing Nb content, since second condensation reactions are favored at high Nb-contents. In addition, the selectivity to ethyl acetate also decreases when increasing Nb concentration (Figure 7b), although this effect seems to be more related to an increase in the yield of condensation products rather than an effective decrease in ethyl acetate formation. In fact, ethyl acetate yield remains almost constant in all the series (Table 2). These observations are in agreement with the specific acid properties of the materials, in which BAS/LAS ratio decreases when increasing Nb content, what would benefit the reactivity via a condensation reaction instead of the esterification reaction (Figure 4c).

**Table 2**

In this context, the catalytic performance of W-Nb-O oxides should be interpreted considering the concentration and the nature of acid sites on the surface of catalysts (Fig. 5). Thus, an increase of the concentration of acid sites in the samples gives rise to an increase in the yield to both the intermediate compounds (2M2P and $C_5$-$C_8$ fraction) and final ($C_9$-$C_{10}$ fraction) products, as well as in the Total organic yield (Figure 7b). The control of BAS/LAS ratio in the catalysts is also an important issue in order to increase the yield to condensation products. On one hand, a very high BAS/LAS ratio (i.e. catalysts with low Nb-contents) does not favor the condensation reactions, neither to reaction intermediates nor to final products ($C_9$-$C_{10}$), leading mainly to esterification and other Brönsted acid catalyzed reactions. On the other hand, higher concentration of Lewis acid sites (i.e. catalysts with high Nb-contents) favors the desired condensation reactions to produce $C_5$-$C_8$ and $C_9$-$C_{10}$ products, being these conditions attained on catalysts with Nb/(W+Nb) ratios above 0.53 (Table 1). Interestingly catalysts with Nb/(W+Nb) ratios of 0.53 or higher lead to products mixtures showing phase

separation, in which compounds with high carbon number are preferentially present in the upper organic phase (Figure S6). Nevertheless, a very high concentration of Lewis acid sites in the catalysts produces the over condensation of $C_9$-$C_{10}$ compounds with indiscriminate growing of the carbon chain to give heavier compounds (i.e. polymers), thus decreasing the amount of the desired $C_5$ to $C_{10}$ range products obtained in the final mixture. Accordingly, an adequate BAS/LAS ratio with an optimized amount of Lewis acid sites is required in the catalyst for the desired condensation reaction to occur. The optimum value is achieved at a Nb/(W+Nb) atomic ratio in the 0.62-0.80 range (Figure 7b) (Table 1).

Catalysts were also tested at higher reaction temperature (200 ºC) (Table S2), whereas Figure 8 compares the catalytic performance of all the catalysts at 180 and 200 ºC. Increasing the reaction temperature improves second condensation reaction steps, as it can be deduced from the decrease in the yield to intermediates (2M2P and $C_5$-$C_8$) and the concomitant increase in the yield to $C_9$-$C_{10}$ products (Figure 8a and 8b).

However, a slight decrease (from ca. 93% to ca 88%) in the carbon balance is also observed at 200 ºC, due to polymerization/over-condensation reactions, that give rise to higher molecular weight compounds, which are not detected by gas chromatography (Table S2).

According to the complexity of the aqueous reaction mixture, additional experiments have been conducted using a simpler feed, containing propanal and ethanol (EtOH), in the presence of $H_2O$ (propanal-EtOH-$H_2O$ weight ratios of 25/45/30) (Figure 9 and Table S3). In this case, the tests were carried out using 50 mg of catalyst during 1h of reaction.

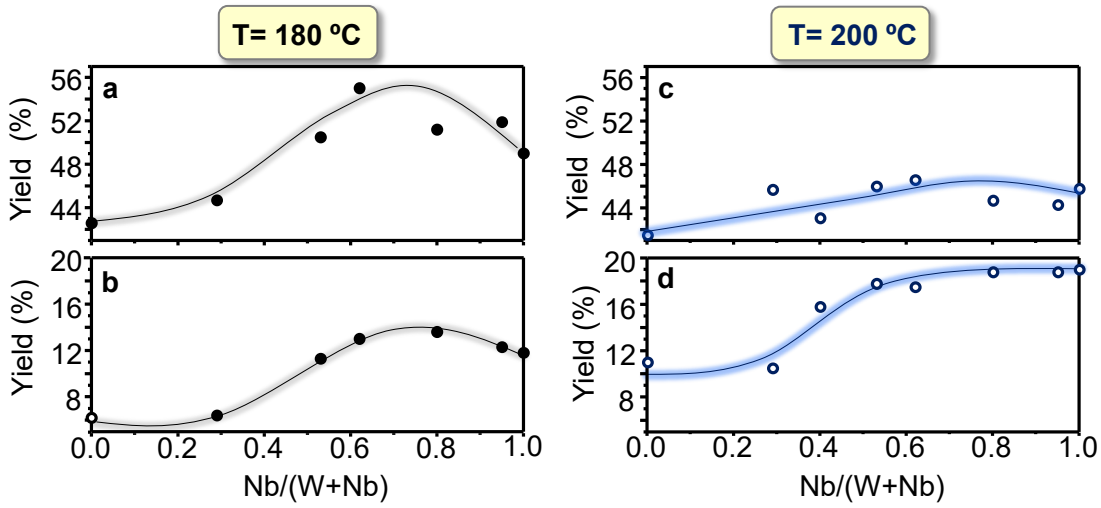


**Figure 8.** Variation of yields to $C_5$-$C_8$ products (a, c) and $C_9$-$C_{10}$ products (b, d) with the Nb-content of catalysts during the reaction at 180 ºC (a, b) and 200 ºC (c, d). Time on stream of 7 h.

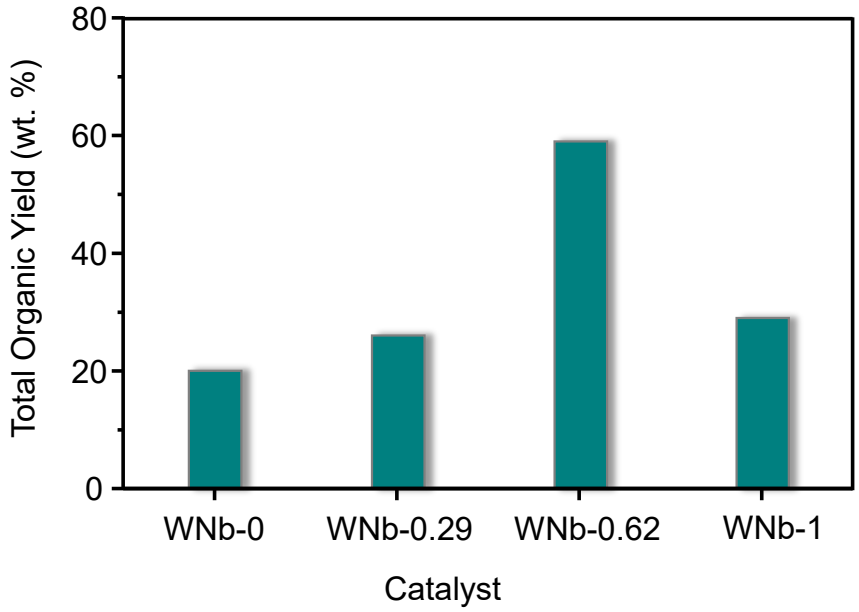


**Figure 9.** Total organic yield during propanal self-aldol condensation on representative W-Nb mixed oxides in the presence of $H_2O$. Reaction conditions: $m_{CAT}$ = 50 mg; reaction time = 1 h; propanal/EtOH/$H_2O$ wt% ratio of 25/45/30.

As observed above for the complex aqueous mixture, catalysts showing a higher Lewis acidity i.e. sample WNb-0.62, display the best catalytic performance, in terms of propanal conversion and total organic yield (Figure 9).

The recyclability of the catalysts was evaluated by performing several consecutive reuses (Figure 10 and Table S4). Studies on the catalyst stability are essential in this case, when dealing with aqueous solutions, especially in acidic media (model aqueous solution containing diverse organic compounds used in this work has a pH = 1.5 due to the high concentration of acetic acid, 30 wt%).

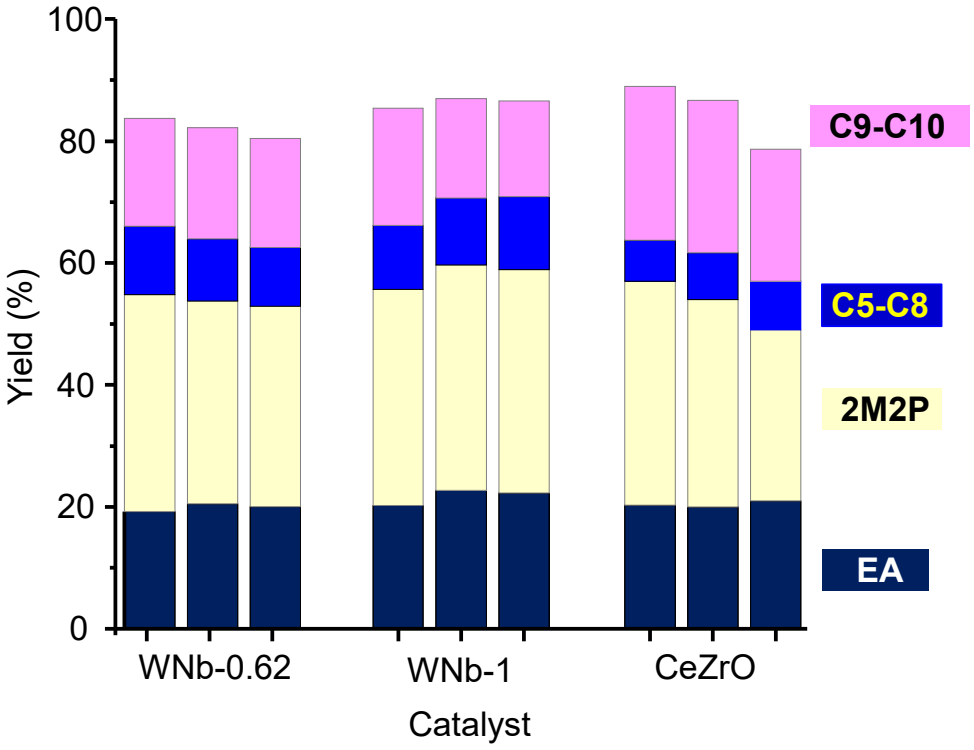


**Figure 10.** Total organic yield and distribution of the main reaction products achieved after several uses over WNb-0.62 and WNb-1. For comparison, the catalytic results over a Ce-Zr-O catalyst have been included. Reaction conditions: 13 bar $N_2$ and 200 ºC under continuous stirring; time on stream of 7 h.

After each cycle, catalysts were separated from the reaction mixture by centrifugation, washed with methanol and dried at 100 ºC overnight. Nb-containing catalysts show a high stability, presenting similar total organic yield after three consecutive uses (Figure 10) (Table S4), with no leaching of the active components.

It is important to note that these recycling results are better than those obtained previously over $Ce_{0.5}Zr_{0.5}O_2$ catalyst,[56] which shows a drastic decrease in the total organic yield after the second use and displayed a loss of ca. 30 wt% of Ce, as it was detected in the liquids after the first use (Table S5).

The catalytic performance of W-Nb mixed oxides have also been compared with other simple oxides, as $ZrO_2$, $CeO_2$, $Al_2O_3$, and $TiO_2$ (anatase and rutile); typically used in aldol-condensation reactions (Figure S7). Figure S7 shows that W-Nb-O catalysts display higher organic yield compared to simple oxides. Only $CeO_2$ catalyst reaches similar catalytic behavior. However, this catalyst is completely dissolved in the reaction media, mainly due to the presence of acetic acid (pH = 1.5).

## 4. CONCLUSIONS

A series of W-Nb-O bronze oxides have been prepared by the hydrothermal method, heat-treated at 550 ºC, and tested in two reactions related to the biomass-derived oxygenates transformation processes that require different acid characteristics: i) the aerobic transformation of glycerol to acrolein; and ii) the valorization of light oxygenates present in an aqueous model mixture simulating an aqueous effluent in a bio-refinery. The crystal structure of W-Nb-O materials corresponds to the HTB-type phase for Nb/(W+Nb) ratios lower than 0.4. Higher Nb-contents progressively eliminates the presence of HTB phase, and periodicity is only assignable to the connectivity between

octahedra. In addition, Nb/(W+Nb) ratios close to 0.5 promote the formation of small crystallites showing a $Cs_{0.5}W_{2.5}Nb_{2.5}O_{14}$ type-phase,[53] isostructural to the so-called M1-phase proposed as active and selective catalysts for the ethane ODH[40] and the partial oxidation of propane.[54] Textural and acid properties can be tuned by controlling the niobium amount. Materials progressively present both higher surface area and higher concentration of acid sites, but lower surface density of acid sites and lower BAS/LAS ratio. In this way, the mesoporosity increases for samples with Nb/(Nb+W) ratios higher than 0.53, which runs in parallel with a narrow pore size distribution and packed agglomeration of uniform nanoparticles.

Hexagonal tungsten bronzes are selective catalysts in the transformation of glycerol to acrolein. Increasing the Nb-content initially favors a higher selectivity to acrolein. The formation of heavy-compounds and carbon oxides, mainly related to higher concentration of Lewis acid sites, is observed at high Nb-contents.

On the contrary, increasing Nb content gives rise to higher yields to first and second condensation products in the valorization of aqueous organic fraction, (close to 70% of Total organic yield). These improved yields can be explained in terms of the specific acid properties of the catalysts. In this sense, the control of both the concentration of acid sites and the BAS/LAS ratio seems to be the key factors for improving the yield to intermediates (2M2P and $C_5$-$C_8$) and final ($C_9$-$C_{10}$) reaction products. The best catalytic performance has been observed for samples with a Nb/(W+Nb) atomic ratio higher than 0.53, the maximum total organic yield being found for a ratio of ca. 0.62 (which seems to present the optimum BAS/LAS ratio).

The effect of temperature of reaction in the valorization of aqueous organic fraction has also been studied, showing a decrease in the yield to intermediates at higher reaction temperatures, since second condensation reactions are favored. This leads to an

increment in the yield to $C_9$-$C_{10}$ products. However, since higher temperatures also favor polymerization/over-condensation reactions, reaction conditions must be optimized. More importantly, the catalysts are stable under reaction conditions, maintaining their catalytic performance after several uses.

The W-Nb-O materials have shown higher stability than Ce-Zr oxide (reference catalyst) and show promising results for further research and application in this type of processes. Interestingly, the heavier fraction ($C_5$ to $C_{10}$ products) formed during light oxygenates condensation spontaneously forms a new upper-organic phase, which separates from aqueous phase, thus reducing further separation and processing costs.

In summary, W-Nb-O mixed oxides shows an outstanding catalytic performance in the aqueous phase transformation of both glycerol and short chain oxygenated compounds mixtures. More interestingly, W-Nb-O mixed oxide bronzes can be stated as very promising systems according to their tailored acid properties, especially for catalytic applications in which a specific Bronsted/Lewis acid sites ratio is necessary to improve the catalytic performance.

## Conflict of interest

There are no conflicts to declare

## Acknowledgments

Financial support by Spanish Government (CTQ-2015-68951-C3-1, CTQ-2015-67592, MAT2016-78362-C4-4-R and SEV-2016-0683) and Generalitat Valenciana (GVA, PROMETEO/2018/006) is gratefully acknowledged. A.F-A. and D.D. thank “La Caixa-

Severo Ochoa" Foundation and Severo Ochoa Excellence Program (SVP-2016-0683), respectively, for their fellowships. Authors thank the ICTS Centro Nacional de Microscopia Electrónica (UCM) for instrumental facilities.

**Notes and References**

1. G. W. Huber, S. Iborra and A. Corma, *Chem. Rev.,* 2006, **106**, 4044-4098.
2. A. Corma, S. Iborra and A. Velty, *Chem. Rev.*, 2007, **107**, 2411-2502.
3. C. O. Tuck, E. Perez, I. T. Horvath, R. A. Sheldon and M. Poliakoff, *Science*, 2012, **337**, 695-699.
4. D. M. Alonso, J. Q. Bond and J. A. Dumesic, *Green Chem.*, 2010, **12**, 1493-1513.
5. G. W. Huber and A. Corma, *Angew. Chem., Int. Ed.,* 2007, **46**, 7184-7201.
6 G. M. Lari, G. Pastore, M. Haus, Y. Ding, S. Papadokonstantakis, C. Mondelli and J. Pérez-Ramírez, *Energy Environ. Sci.,* 2018, **11**, 1012-1029.
7 D. Sun, Y. Yamada, S. Sato and W. Ueda, *Green Chem.,* 2017, **19**, 3186-3213.
8 D. Cespi, F. Passarini, G. Mastragostino, I. Vassura, S. Larocca, A. Iaconi, A. Chieregato, J. L. Dubois and F. Cavani, *Green Chem.*, 2015, **17**, 343-355.
9 B. Katryniok, S. Paul, V. Bellière-Baca, P. Rey and F. Dumeignil, *Green Chem.*, 2010, **12**, 2079-2098.
10 R. Venderbosch and W. Prins, *Biofuel. Bioprod. Bior.,* 2010, **4**, 178-208.
11 I. Graça, J. M. Lopes, H. S. Cerqueira and M.F. Ribeiro, *Ind. Eng. Chem. Res.,* 2013, **52**, 275-287.
12 M. Asadieraghi, W. M. A. Wan Daud and H. F. Abbas, *Renew. Sust. Energ. Rev.,* 2014, **36**, 286-303.
13 A. Pinheiro, D. Hudebine, N. Dupassieux and C. Geantet, *Energy Fuels,* 2009, **23**, 1007-1014.
14 V. N. Bui, G. Toussaint, D. Laurenti, C. Mirodatos and C. Geantet, *Catal. Today,* 2009, **143**, 172-178.
15 F. Wang, J. L. Dubois and W. Ueda. *Appl. Catal. A: Gen.*, 2010, **376**, 25-32.
16 G. S. Foo, D. Wei, D. S. Sholl and C. Sievers, *ACS Catal.,* 2014, **4**, 3180−3192.
17 F. G. E. Nogueira, Y. J. O. Asencios, C. B. Rodella, A. L. M. Porto and E. M. Assaf, *Mater. Chem Phys.*, 2016, **184**, 23-30.

18 M. Massa, A. Andersson, E. Finocchio and G. Busca, *J. Catal.*, 2013, **307**, 170-184.

19 M. Massa, A. Andersson, E. Finocchio, G. Busca, F. Lenrick and L. R. Wallemberg, *J. Catal.*, 2013, **297**, 93-109.

20 a) M. Dalil, D. Carnevali, J. L. Dubois and G. S. Patience, *Chem. Eng. J.*, 2015, **270**, 557-563; b) M. Dalil, D. Carnevali, M. Edake, A. Auroux, J. L. Dubois and G. S. Patience, *J. Mol. Catal. A: Chem.*, 2016, **421**, 146-155.

21 M. D. Soriano, P. Concepcion, J. M. Lopez Nieto, F. Cavani, S. Guidetti and C. Trevisanut, C. *Green Chem.,* 2011, **13**, 2954-2962.

22 T. Murayama, K. Nakajima, J. Hirata, K. Omata, E. J. M. Hensen and W. Ueda, *Catal. Sci. Technol.,* 2017, **7**, 243-250.

23 N. La Salvia, D. Delgado, L. Ruiz-Rodríguez, L. Nadji, A. Massó and J. M. Lopez Nieto, *Catal. Today,* 2017**, 296**, 2-9.

24 A. Chieregato, F. Basile, P. Concepción, S. Guidetti, G. Liosi, M. D. Soriano, C. Trevisanut, F. Cavani and J. M. López Nieto, *Catal. Today*, 2012, **197**, 58-65.

25 A. Chieregato, M. D. Soriano, E. García-González, G. Puglia, F. Basile, P. Concepción, C. Bandinelli, J. M. López Nieto and F. Cavani, *ChemSusChem,* 2015**, 8**, 398-406.

26 A. Chieregato, C. Bandinelli, P. Concepción, M. D. Soriano, F. Puzzo, F. Basile, F. Cavani and J. M. Lopez Nieto, *ChemSusChem,* 2017**, 10**, 234-2446.

27 J. J. Deleplanque, J. L. Dubois, J. F. Devaux and W. Ueda, *Catal. Today*, 2010, **157**, 351–358.

28 D. Delgado, A. Chieregato, M. D. Soriano, E. Rodriguez-Aguado, L. Ruiz-Rodriguez, E. Rodriguez-Castellon and J. M. López Nieto, *Eur. J. Inorg. Chem.,* 2018, **2018** (10), 1204-1211.

29 T. N. Pham, T. Sooknoi, S. P. Crossley and D. E. Resasco, *ACS Catal.,* 2013, **3**, 2456-2473.

30 L. Faba, E. Díaz and S. Ordóñez, *ChemSusChem,* 2014, **7**, 2816-2820.

31 C. A. Gaertner, J. C. Serrano-Ruiz, D. J. Braden and J. A. Dumesic, *J. Catal.,* 2009, **266**, 71-78.

32 A. Gangadharan, M. Shen, T. Sooknoi, D. E. Resasco and R. G. Mallinson, *Appl. Catal. A: Gen.,* 2010, **385**, 80-91.

33 a) S. Wang and E. Iglesia, *J. Catal.,* 2017, **345**, 183-206; b) S. Wang, K. Goulas and E. Iglesia, *J. Catal.,* 2016, **340**, 302-320.

34 M. E. Domine, J. M. López Nieto, D. Delgado and A. Fernández-Arroyo, WO2017/162900 A1, **2017**.

35 A. Fernández-Arroyo, D. Delgado, M. E. Domine and J. M. López Nieto, *Catal. Sci. Technol.,* 2017*,* **7**, 5495-5499.

36 K. Nakajima, J. Hirata, M. Kim, N. Gupta, T. Murayama, A. Yoshida, N. Hiyoshi, A. Fukuoka and W. Ueda, *ACS Catal.,* 2018, **8**, 283-290.

37 Y. Goto, K.-i. Shimizu, K. Kon, T. Toyao, T. Murayama and W. Ueda, *J. Catal.,* 2016, **344**, 346-353.

38 K. Omata, K. Matsumoto, T. Murayama and W. Ueda, *Catal. Today,* 2016**, 259**, 205-212.

39 N. Blanch-Raga, M. D. Soriano, A. E. Palomares, P. Concepción, J. Martínez-Triguero and J. M. López Nieto, *Appl. Catal. B- Environ.,* 2013, **130-131**, 36-43.

40 P. Botella, E. García-González, A. Dejoz, J. M. López Nieto, M. I. Vázquez and J. González-Calbet, *J. Catal.*, 2004, **225**, 428–438

41 Y. Yun, J. R. Araujo, G. Melaet, J. Baek, B. S. Archanjo, M. Oh, A. P. Alivisatos and G. A. Somorjai, *Catal. Lett.,* 2017, **147**, 622-632.

42 Y. S. Yun, K. R. Lee, H. Park, T. Y. Kim, D. Yun, J. W. Han and J. Yi, *ACS Catal.,* 2015, **5**, 82-94.

43 M. D. Soriano, A. Chieregato, S. Zamora, F. Basile, F. Cavani and J. M. López Nieto, *Top. Catal.,* 2015, **59**, 178-185.

44 L. Nadji, A. Massó, D. Delgado, R. Issaadi, E. Rodríguez-Aguado, E. Rodríguez-Castellón and J. M. López Nieto, *RSC Adv.*, 2018, **8**, 13344-13352.

45 C. A. Emeis, *J. Catal.,* 1993**, 141**, 347-54.

46 T. Murayama, N. Kuramata, S. Takatama, K. Nakatani, S. Izumi, X. Yi and W. Ueda, *Catal. Today,* 2012, **185**, 224-229.

47 H. Hibst, F. Rosowski and G. Cox, *Catal. Today,* 2006, **117**, 234-241.

48 R. D. Shannon, *Acta Cryst.,* 1976, A32, 751.

49 I. M. Szilágyi, J. Madarász, G. Pokol, P. Király, G. Tárkányi, S. Saukko, J. Mizsei, A. L. Tóth, A. Szabó and K. Varga-Josepovits, *Chem.Mater.,* 2008, **20**, 4116-4125.

50 M. Maczka, J. Hanuza, S. Kojima, A. Majchrowski and J. H. Van der Maas, *J. Raman Spectrosc.,* 2001, **32**, 287-291.

51 A. A. McConnell, J. S. Anderson and C. N. R. Rao, *Spectrochim. Acta,* 1976**, 32A**, 1067-1076.

52 J. M. Jehng and I. E. Wachs, *Chem. Mater.,* 1991, **3**, 100-107.

53 J. M. Jehng and I. E. Wachs, *ACS Symp. Ser.,* 1990, **437**, 232-42.

54 M. D. Soriano, E. Garcia-Gonzalez, P. Concepcion, C. B. Rodella and J. M. Lopez Nieto, *Cryst. Growth Des.,* 2017, **17**, 6320-6331.

55 K. Oshihara, T. Hisano and W. Ueda, *Top. Catal.,* 2001, 15, 153-160.

56 A. Gangadharan, M. Shen, T. Sooknoi, D. E. Resasco and R. G. Mallinson, *Appl. Catal. A: Gen.,* 2010, **385**, 80-91.

57 K. Suwannakarn, E. Lotero and J. G. Goodwin, *Ind. Eng. Chem. Res.,* 2007, **46**, 7050-7056.

**Table 1.** Physicochemical Features of W-Nb-O Mixed Oxides Catalysts.

| Sample | Nb/(W+Nb) atomic ratio in bulk solid [a] | Nb/(W+Nb) in the synthesis gel | $S_{BET}$ ($m^2\ g^{-1}$) [b] | Pore size (nm) [c] | Mesopore volume ($cm^3\ g^{-1}$) [c] | Concentration of acid sites ($\mu mol_{py}\ g^{-1}$) [d] | Surface density of acid sites ($\mu mol_{py}\ m^{-2}$) [d] | BAS/LAS [d] |
|---|---|---|---|---|---|---|---|---|
| WNb-0 | 0.00 | 0.00 | 28 | 17.2 | 0.045 | 27.4 | 0.98 | 0.7 |
| WNb-0.29 | 0.29 | 0.25 | 38 | 11.1 | 0.050 | 29.7 | 0.78 | 1.8 |
| WNb-0.40 | 0.40 | 0.35 | 67 | 13.6 | 0.095 | 56.2 | 0.84 | 1.1 |
| WNb-0.53 | 0.53 | 0.50 | 102 | 14.6 | 0.176 | 73.2 | 0.71 | 1.2 |
| WNb-0.62 | 0.62 | 0.59 | 124 | 5.9 | 0.216 | 89.2 | 0.70 | 0.5 |
| WNb-0.80 | 0.80 | 0.80 | 129 | 5.4 | 0.192 | 122.3 | 0.95 | 0.7 |
| WNb-0.95 | 0.95 | 0.95 | 129 | 3.7 | 0.130 | 62.2 | 0.48 | 0.4 |
| WNb-1 | 1.00 | 1.00 | 70 | 3.5 | 0.061 | 36.4 | 0.54 | 0.8 |

[a] As determined by XEDS. [b] Calculated from $N_2$ adsorption isotherms. [c] Calculated by BJH method. [d] From FTIR of adsorbed pyridine.

**Table 2**. Catalytic Results in the Valorization of the Aqueous Model Mixture over W-Nb-O Catalysts at 180 ºC. [a]

| Sample | Total organic yield (%) | Conversion (%) | | | | Selectivity (%) | | | | Carbon balance (%) |
|---|---|---|---|---|---|---|---|---|---|---|
| | | Acetol | Propanal | Ethanol | Acetic acid | $C_5$-$C_8$ | $C_9$-$C_{10}$ | 2M2P [b] | Ethyl acetate | |
| WNb-0 | 49.2 | 100 | 61.2 | 40.4 | 17.2 | 19.5 | 8.6 | 38.1 | 33.8 | 96.5 |
| WNb-0.29 | 51.5 | 100 | 77.8 | 38.0 | 15.2 | 21.2 | 8.8 | 38.7 | 31.3 | 94.8 |
| WNb-0.53 | 62.2 | 100 | 84.5 | 43.4 | 13.3 | 18.5 | 13.3 | 40.2 | 28.0 | 92.1 |
| WNb-0.62 | 68.4 | 100 | 90.1 | 47.2 | 17.8 | 17.6 | 14.3 | 42.3 | 25.8 | 96.7 |
| WNb-0.80 | 65.2 | 100 | 84.0 | 36.7 | 19.9 | 13.3 | 15.7 | 45.2 | 25.7 | 97.1 |
| WNb-0.95 | 64.6 | 100 | 89.7 | 43.3 | 13.7 | 11.4 | 13.9 | 46.3 | 28.4 | 96.4 |
| WNb-1 | 61.2 | 100 | 80.3 | 40.9 | 18.1 | 16.3 | 14.2 | 41.8 | 27.7 | 95.6 |

[a] Reaction conditions: aqueous model mixture (3.0 g) and catalyst (0.15 g) in autoclave-type reactor, at 13 bar (under $N_2$) and 180 ºC under continuous stirring during 7 h. [b] 2M2P = 2-methyl-2-pentenal.

## Caption to Figures

**Fig. 1**. A) XRD patterns of W-Nb-O catalysts. a) WNb-0; b) WNb-0.29; c) WNb-0.40; d) WNb-0.53; e) WNb-0.62; f) WNb-0.80; g) WNb-0.95; h) WNb-1. Miller indices have been assigned according to the hexagonal $WO_3$ phase (*h*-$WO_3$ JCPDS: 00-33-1387). B) Projected structural model of the *h*-$WO_3$ structure along the [001] and [210] directions. C) Variation of *c*-axis as a function of Nb content.

**Fig. 2**. Raman spectra of W-Nb-O catalysts: a) WNb-0; b) WNb-0.29; c) WNb-0.40; d) WNb-0.53; e) WNb-0.62; f) WNb-0.80; g) WNb-0.95; h) WNb-1.

**Fig. 3.** (a) Electron diffraction ring pattern for the WNb-0.29 sample; (b) High resolution image showing a group of representative crystals of WNb-0.29; (c) Electron diffraction ring pattern for the WNb-0.53 sample; (d) High resolution micrograph showing several crystallites of this catalyst; (e) High resolution image showing one crystallite (pointed by the black arrow) in which fragments of the $Cs_{0.5}Nb_{2.5}W_{2.5}O_{14}$ type phase can be recognized; (f) Projected structure model of $Cs_{0.5}Nb_{2.5}W_{2.5}O_{14}$ type phase along the [001] direction; (g) Electron diffraction ring pattern corresponding to the WNb-0.80 sample; (h) High resolution image showing several crystallites of WNb-0.80. Miller index in all diffraction patterns have been assigned on the basis of the HTB-type phase (ICDD: 00-33-1387).

**Fig. 4.** Acid features of W-Nb-O mixed oxides catalysts obtained by FTIR of adsorbed pyridine: a) Concentration of acid sites sites (in $\mu mol_{py}\ g^{-1}$); b) Surface density of acid sites (in $\mu mol_{py}\ m^{-2}$); and c) BAS/LAS ratio (BAS: Brönsted Acid Sites; LAS: Lewis Acid Sites).

**Fig. 5**. TPD-$NH_3$ profiles of W-Nb-O catalysts: a) WNb-0; b) WNb-0.29; c) WNb-0.40; d) WNb-0.53; e) WNb-0.62; f) WNb-0.80; g) WNb-0.95; h) WNb-1.

**Fig. 6**. Variation of the yield to the main reaction products (acrolein, $CO_X$ and heavy-compounds) as a function of Nb content in catalyst**.** Reaction condition**s**: glycerol/$H_2O$/$O_2$/He molar ratio of 2/40/4/54, T = 295 ºC, Contact time, W/F, of 81 $g_{cat}\ h\ (mol_{gly})^{-1}$.

**Fig. 7**. Variation of the conversion of each reactant in the aqueous model mixture (i.e. acetol, propanal, ethanol and acetic acid) (a) and variation of selectivity to the main products (i.e. 2-methyl-2-pentenal, ethyl acetate, and $C_5$-$C_8$ and $C_9$-$C_{10}$ compounds) (b) as a function of Nb content in catalyst**.** Reaction conditions: Aqueous model mixture (3.0 g) and catalyst (150 mg) in autoclave-type reactor, at 13 bar $N_2$ and 180˚C under continuous stirring; time on stream of 7 h.

**Fig. 8**. Variation of yields to $C_5$-$C_8$ products (a) and $C_9$-$C_{10}$ products (b) with the Nb-content of catalysts during the reaction at 180 ºC and 200 ºC. Time on stream of 7 h.

**Fig.9.** Total organic yield during propanal self-aldol condensation on representative W-Nb mixed oxides. Reaction conditions: $m_{CAT}$ = 50 mg; propanal-EtOH-$H_2O$ weight ratio of 25/45/30 and a time of stream of 1h..

**Fig. 10**. Total organic yield and distribution of the main reaction products achieved after several uses over WNb-0.62 and WNb-1. For comparison, the catalytic results over a Ce-Zr-O catalyst have been included. Reaction conditions: 13 bar $N_2$ and 200 ºC under continuous stirring; time on stream of 7 h.